Deliverable 2.4 Examination & interpretation of the seismic tomography data in respect to "up-lift" phenomena and stress-induced anisotropy

Digital monitoring of CO2 storage projects

Prepared by

Uta Koedel (Geotomographie GmbH)

Thomas Fechner (Geotomographie GmbH)

DigiMon Deliverable D.2.4 Version 1.2

March 2022

The Digimon, project no 299622 is supported by the ACT international initiative http://www.act-ccs.eu/about-us and funded by GASSNOVA (NO), RCN (NO), BEIS (UK), Forschungszentrum Jülich (DE), GSRT (GR), RVO (NL), UEFISCDI (RO), DoE (US), Repsol Norge (NO) and Equinor (NO)

Revision

Version	Date	Change	Page
1.0	15.03.2022	First version	All
1.1	17.03.2022	Explain CCS, add some explaination	4,5,25
1.2	23.06.2022	Revision after reviewers comments	All

Document distribution

ACT Coordinator

- Research Council of Norway

ACT national funding agencies

- Forschungszentrum Jülich GmbH, Projektträger Jülich, (FZJ/PtJ), Germany.
- Geniki Grammatia Erevnas kai Technologias/The General Secretariat for Research and Technology (GSRT), Greece.
- Ministry of Economic Affairs and Climate/Rijksdienst voor Ondernemend Nederland (RVO), the Netherlands.
- The Research Council of Norway (RCN), Norway.
- Gassnova, Norway.
- Development and Executive Agency for Higher Education, Research, Development and Innovation Funding (UEFISCDI), Romania.
- Department for Business, Energy and Industrial Strategy (BEIS), U.K.
- Department of Energy (DoE), USA.

DigiMon partners

- NORCE Norwegian Research Centre AS
- OCTIO Environmental Monitoring AS
- NTNU Norwegian University of Science and Technology
- University of Bristol
- University of Oxford
- CRES Centre for Renewable Energy Sources and Saving
- Helmholtz–Centre for Environmental Research
- Sedona Development SRL
- TNO Nederlandse Organisatie voor toegepast -natuurwetenschappelijk Onderzoek
- Geotomographie GmbH
- LLC Lawrence Livermore National Security
- SILIXA LTD
- EQUINOR ASA
- REPSOL –NORGE AS

Table of content

1 Introduction

In recent years, global concerns about greenhouse gas emissions have stimulated considerable interest in carbon capture and storage (CCS) as a climate change mitigation option that can be used to reduce man-made CO_2 emissions. This is achieved by separating and capturing CO_2 from emission sources, then injecting and storing it in the subsurface. However, CCS requires the secure retention of CO_2 in geological formations over thousands of years. To achieve this, there are two distinct purposes for undertaking monitoring at CO_2 storage sites: (1) to ensure conformance by tracking the pressure buildup and CO_2 inside the storage complex, thereby helping to indicate the long term security of the site ('integrity monitoring') and (2) to ensure containment by triggering timely control measures to mitigate any unexpected leakage, helping to demonstrate the current security situation, especially in the area surrounding the storage complex ('assurance monitoring') (Bourne et al. 2014).

A significant issue for storage security is the geomechanical response of the reservoir. Concerns have been raised that geomechanical deformation induced by CO_2 injection connected with pressure increase will create or reactivate fracture networks in the sealing caprocks, providing a pathway for CO_2 leakage (Verdon et al. 2013). Several geochemical and geophysical (such as time-lapse seismic) techniques allow monitoring the regional distribution of CO_2 in the storage complexes, seal integrity and the pressure evolution in response to the injection and therefore can be used to verify storage conformance and are valuable tools for integrity monitoring (IEA 2012).

The most significant environmental risk associated with CCS technology is gradual leakage through undetected faults, fractures, or wells, or the potential problems caused by leakages due to injection well failure or leakages up through an abandoned well. In addition, other issues include the influence of a CO_2 plume, reservoir pressure changes, and geomechanical changes in the multilayered subsurface with minor and major faults as migration paths. There are injection-induced stress, strain, deformations, and potential microseismic events resulting from changes in reservoir pressure and temperature and unwanted unelastic mechanical changes that might reduce sequestration efficiency and cause concerns in the local community.

Figure 1: Geomechanical processes and critical technical issues associated with Carbon Capture and Storage (CCS) in deep sedimentary formations (Nicol et al. 2016).

In Salah Gas Project is well known as one of the huge CCS (Carbon dioxide Capture and Storage) projects in the world where the CO_2 is separated from natural gas produced from three fields of Krechba, Reg, and Teguentour, and is injected underground at three wells down-dip from the Krechba natural gas accumulation. The field is located in the rocky desert where the ground surface is vegetation-free. Surface deformation around CO_2 injection wells at In Salah, Algeria, was analyzed by satellite-borne Synthetic Aperture Radar (SAR) data by Onuma & Ohkawa (2009). Verdon et al. (2013) reported that pore pressures have increased significantly in In Salah, leading to substantial geomechanical deformation that has uplifted the surface by 2 cm, generated thousands of microseismic events, and appears to have reactivated a fracture network extending from the reservoir 100–200 m into the overburden. Stork et al. (2015) reported that the observation and analysis of microseismicity recorded at the In Salah CO2 sequestration site exhibits little variation in characteristics throughout the monitoring period, 2009–2011. Although thousands of events are recorded, they occur in clusters with similar waveforms and apparently collocated hypocentres.

Seismic is used as one method to monitor these geomechanical deformations. For example, at Sleipner, time-lapse seismic have been used to determine the pressure change in the reservoir (Chadwick et al. 2012). In producing oilfields, changes in the travel time above the reservoir have been used to infer stress transfer into the overburden (Hatchell & Bourne 2005; Staples et al. 2007). Similarly, azimuthal variations in seismic attributes (Duxbury et al. 2012) and S-wave splitting (Olofsson et al. 2003) have been used to image the creation and reactivation of fracture networks due to reservoir deformation.

Time-lapse seismic monitoring has been applied at different CCS sites. The Sleipner field (Arts et al., 2008; Boait et al., 2012; Eiken, 2019), the In Salah storage project (Gibson-Poole & Raikes, 2010; Zhang et al., 2015) and the EOR project at Weyburn (White et al., 2011; White, 2013a, 2013b), as well as at the Aquistore field site (White et al., 2015).

In this deliverable the potential of conventional seismic measurements to characterize such phenomena is discussed.

2 Interlinkage between injection and up lift phenomena

2.1 Recent knowledge

Ground displacements are generally understood as either the uplifting or subsidence of the earth's surface areas, usually gradually. These displacements can be evidence of several processes of natural origin such as swelling/shrinkage of expansive soils, compaction of recent deposits, tectonic displacements associated with the occurrence of earthquakes or long-term tectonic movements, and anthropogenic causes such as pumping-induced aquifer-system compaction (Bonì et al. 2018, Galloway et al. 1999). In some places, gradual compaction of loose sediments results in natural displacement. However, most of the displacements are man-made. These man-made ground displacements are a well-known phenomenon in traditional mining areas due to groundwater extraction, geothermal projects, or large-scale building development (INSIDE, 2022). In many instances, the movements are due to the interactions of multi-driving factors that act at various spatial and temporal scales (Chaussard et al. 2017).

Furthermore, ground motion can imply surface deformation with 3D displacement components negative and positive vertical and/or horizontal (E-W) movements. Negative displacement corresponds to lowering the earth's surface named land subsidence; meanwhile, positive displacement is the uplift of the earth's surface. Uplift phenomena are less common and less studied than land subsidence. Positive movements (uplift) can occur as a result of various natural and human causes; for example, swelling of clay soils (Deffontaines et al. 2015), fault effects (Amelung et al. 1999), and

water rebound in mining areas (Bateson et al. 2015, Gee et al. 2017). These uplift phenomena can lead to various environmental and engineering problems such as springs of polluted water (Johnston et al. 2008) and damage to building foundations (Brake et al. 2019, Kurka et al. 2015).

The injection of fluid (water, gas, vapor) into the subsurface occurs worldwide for a variety of purposes, e.g., to enhance oil production (EOR), store gas in depleted gas/oil fields, enhancement of overloaded aquifer storage and recovery systems (ASR) and attempts to mitigate anthropogenic land subsidence. Irrespective of the injection target, some areas have experienced an observed land uplift ranging from a few millimeters to tens of centimeters over a time period of a few months to several years depending on the quantity and spatial distribution of the fluid used, pore pressure increase, geological setting (depth, thickness, and area extent), and hydro-geomechanical properties of the injected formation (Teatini et al. 2011).

It is known that changes (even small) in reservoir pressure and temperature induce some stress-and-strain changes in and around the injection zone. This may result in detectable ground-surface deformations and could also lead to noticeable changes in permeability and injectivity. Moreover, the injection-induced fluid pressure and straining of the reservoir and surrounding rock may result in small seismic events that geophones could detect. Even a small pressure change and straining of the rock might result in small microseismic events because of rock heterogeneities, including fractures and local stress concentrations that could be released locally. Such microseismic events can be triggered under the right circumstances, depending on in situ stress, injection pressure, the existence and nature of fractures, and rock properties. As will be further discussed, these types of geomechanical responses, including ground-surface uplift and microseismic events, have been observed at CO_2 storage sites as well as in other types of underground injection operations and are generally useful for monitoring of subsurface fluid flow and geomechanical processes (Mathieson et al., 2011; Teatini et al., 2011; Burch et al., 2009).

2.2 Physical characteristics regarding up-lift phenomena

As soon as fluid injection starts, changes in reservoir stresses and strains can quickly propagate laterally within the injection zone, along with expanding fluid pressure. The pressurization causes vertical expansion of the reservoir and changes in the stress field. These induced changes are, in general, proportional to the magnitude of the pressure increase, ΔP, depending on the geometry and geomechanical properties (such as compressibility) of the reservoir and surrounding sediments. The magnitude of uplift will also depend on the thickness of the underground reservoir pressurized at depth. For example, the possibility of CO_2 or water injection into a saline sandy aquifer lying 600 to 800 m under the lagoon of Venice, Italy, has been suggested for lifting Venice from the sea, an estimated 30 cm (Abbot, 2004; Comerlati et al., 2006; Castelletto et al., 2008). As reported in the introduction chapter at the In Salah CO_2 storage project, around 2.5 cm of uplift have been observed due to CO_2 injection.

2.3 Methods to study subsidence

Several methods study the gentle settlement of the ground surface due to the consolidation of compressible sediments or the loss of regional earth materials due to various processes. First, GPS or tiltmeter can measure land subsidence (e.g. Karegar et al. 2015). Second, differential synthetic aperture radar interferometry (D-InSAR) spaceborne-based is a remotely sensed technology that enables investigation of widespread surface deformation across the earth. To date, the advanced multitemporal InSAR (MT-InSAR) technology allows the measurement of surface deformation with centimeter and even subcentimeter accuracy at very high spatial resolution. It has been widely applied to monitor deformation of the earth's surface, including volcanoes and seismic activity, landslides, glacial motion, mining-related subsidence, subsidence of urban or peri-urban areas, and even large-scale land deformation nationwide (Liu et al., 2021, Meyer et al., 2015; Dong et al., 2019; Necsoiu et al., 2016; Zhang et al., 2015; Castellazzi et al., 2016; Zuo et al., 2019; Costantini et al., 2017). This remote sensing technology is not considered and implemented in the DIGIMON project.

Third, distributed fiber optic strain sensing (DFOSS) has been introduced as an effective tool to detect subsurface deformation continuously (Amer et al., 2021).

Fourth, it has long been known that seismic velocities are also stress-sensitive. Therefore, accurate time-lapse surveys can also be used to image changes in seismic velocity induced by geomechanical deformation, and extension or compaction of the overburden can be imaged by travel time shifts through these areas. (Verdon et al.,2013; Hatchell and Bourne, 2005; Staples et al. 2007).

2.4 Relevant geotechnical parameter

Shear waves react sensitively to changes in dynamic soil parameters such as shear strength or Young's modulus. Due to the heterogeneous structure of the soil, these parameters also have a 3-dimensional nature. During its formation, the soil is exposed to different loading conditions. This can be, for example, the loading pressure due to sedimentation, glaciation, external static load from structures, lowering the groundwater table, or even desiccation. Depending on the soil, these states are conserved and influence the propagation of seismic waves, especially the two different kinds of shear waves. SV- and SH-waves cause rock particles to oscillate perpendicular to the direction that the wavefront is moving, with the SH- and SV-displacement vectors orthogonal to each other.

In geotechnical engineering, the stress history of soil is described by the so-called overconsolidation ratio (OCR) or overconsolidation difference (OCD). The OCR is defined as the ratio of the maximum overburden stress ever experienced by the soil (i.e., with the ice sheet on top) to the present overburden stress (i.e., without the ice sheet) and allows the characterization of the stress history of soils. An overconsolidated soil has experienced more significant stresses in the past than currently exists.

Overconsolidation has a significant influence on shear strength. It causes an increase in strength, reduction in permeability, and a reduction in the settlement. Overconsolidated soils are also usually stiffer and have less settlement. According to Roesler (1979), the stress-induced anisotropic S-wave velocity Vs can be expressed as follows:

$$v_s = C(\sigma_x')^{nx}(\sigma_y')^{ny}$$

where σ_x' is the principal effective stress in the direction of wave propagation and σ_y' is the principal effective stress in the direction of wave polarization. C, nx and ny are material constants.

3 Seismic velocity and up-lift phenomena

3.1 Changes in seismic velocity

An increase in seismic velocity with depth is a typical rock property encountered practically everywhere. Overburden pressure increases vertical stress, producing a nonlinear elastic response (Korneev and Glubokovskikh,2013). Induced stress affects seismic wave propagation in two ways. First, it modifies the equation of motion, and therefore the equation of conservation of linear momentum gains terms related to the induced deviatoric stress. Second, the elastic constitutive relationship acquires terms linear in the induced stress (Tromp et al. 2015). Landro et al. (2003) showed a relationship between changes in P-wave velocity change and change in effective pressure. A typical curve for P-wave velocity versus effective pressure changes is displayed in Figure 2. Landro et al. (2003) reported a similar trend for the S-wave velocity versus effective pressure.

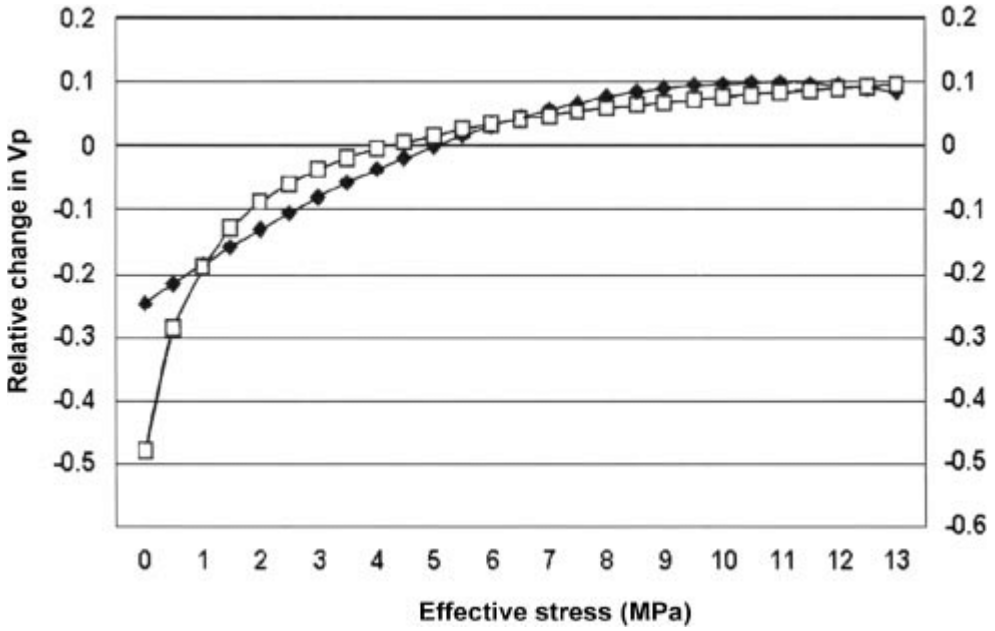

Figure 2: Relative P-wave velocity change versus change in net effective pressure (line with squares) and the second-order approximation used in the data example (line with diamonds). (Landro et al., 2003)

Other studies show that shear-wave velocities are sensitive in-situ indicators of the triaxial stress state of the rock (Winterstein and Meadows, 1991). However, the analysis of S-wave velocity variation with stress state is more complex than the corresponding analysis for P-waves because the S-wave velocities in anisotropic media vary not only as a function of propagation wave direction but also depend on the polarization of the propagating wave (Herwanger & Horne, 2009). Herwanger & Horne (2009) found out that the largest S-wave velocity increase occurs for shear waves that are polarized in the direction of the largest stress increase, while the largest slowdown decrease in P-wave seismic velocity occurs in the direction of the most considerable stress increase.

3.2 Other parameters for interpretation

Depending on the different static stress states of soil, SH and SV waves generated by a crosshole test have individual site-specific velocities. Thus, the in-situ information of the pairwise shear wave velocity profiles (SH and SV) can be used as an approach to evaluate the loading history of soils (Mackens et al. 2017). According to Ku and Mayne (2014) one approach to represent the stress history is through the OCD, which is related to OCR as follows:

$$OCR = (OCD + \sigma'_{y0})/\sigma'_{v0}$$

where σ'_{y0} is the effective overburden stress. OCD is strongly correlated to the paired stiffness ratio ($G_{0,HH}/G_{0,VH}$). The small strain shear modulus, G0, is determined by the shear wave velocity (V_s) measurements

$$G_{0;ij} = \rho_t V_{s;ij}$$

with $G_{0,ij}$ the small strain shear modulus in the 'i-j' soil plane, $V_{s,ij}$ the shear wave velocity in the i propagation direction and in j polarization direction, and ρ_t the total mass density of the soil medium. According to Ku and Mayne (2014) the OCD can be calculated with

$$OCD = 0.466(\sigma_{atm})(\frac{G_{0,HH}}{G_{0,VH}})^{5.77}$$

where σ_{atm} is the reference atmospheric pressure.

The horizontally polarized shear wave borehole source BIS-SH produces the velocity of horizontally propagating and SH-polarized shear waves ($V_{s,HH}$) and the vertically polarized shear wave borehole source BIS-SV the velocity of horizontally propagating and vertically polarized shear waves ($V_{s,HV}$). Supposing a transverse isotropy along the vertical axis, we assumed that $V_{s,VH}$ and $V_{s,HV}$ are identical and used to calculate values of OCD.

Also, the SV/SH velocity ratio can indicate an anisotropic material behavior due to preconsolidation in the course of the geological history.

3.3 Special considerations for shear wave data processing

Uncertainty in picking arrival times is a primary factor. Usually, phase picking often becomes inconsistent and ambiguous due to rather complex waveform patterns. In general, the shape of a seismic wavelet is affected by the source time function, the radiation pattern, dispersion, attenuation, scattering, interference with other phases, the signal-to-noise ratio (SNR) at the recording site, and the response characteristic of the recording system. The superposition of these components may lead to highly complex waveforms in the case of high-frequency local and regional recordings. In the case of interbeds of sand and silt, the signal quality may degrade, and the shear wave identification is not always clearly feasible due to the lack of polarity change. In general, the data quality of the S-wave is defined by its amplitude, which, assuming the same strain modulus, is higher the lower the shear modulus of the subsoil and vice versa. Since the shear modulus of the sand-silt mixture is higher than in the overlying unconsolidated sediment (sand/gravel or clay/silt), lower amplitudes are recorded here.

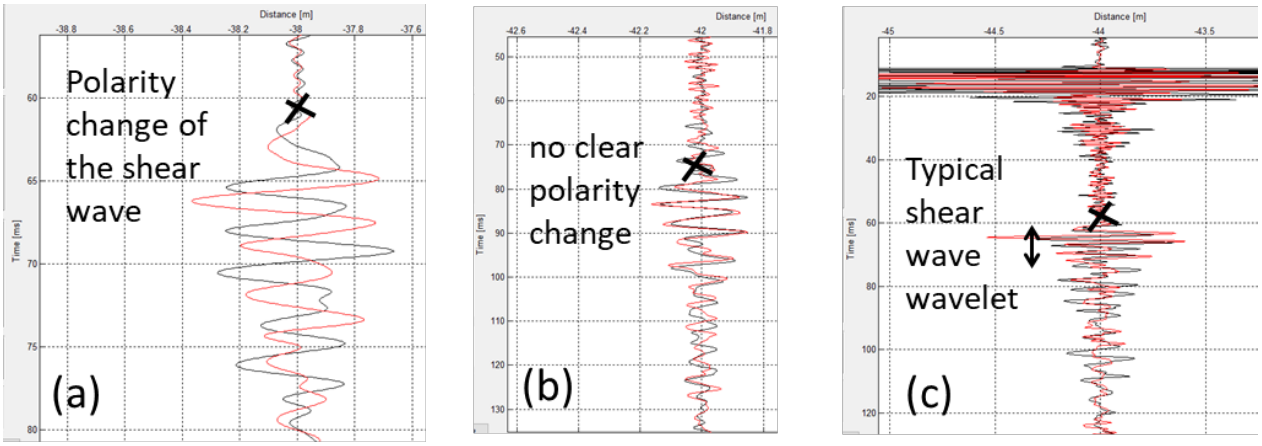

Figure 3: First identification of S-wave arrival time using the polarity change at a depth of 38 m below ground surface (a) and using its typical wavelet shape and high amplitudes at a depth of 52 m (b) and 44m (c) below ground surface. (b) indicates no clear polarity change but shows the typical wavelet.

Due to the lack of polarity reversal of the S-wave in some areas, further criteria had to be used for shear wave identification. Since the S-wave with its high amplitudes is generally clearly different from the P-wave, characterized by high frequencies, and often forms a typical wavelet shape, these features could be used to identify shear waves.

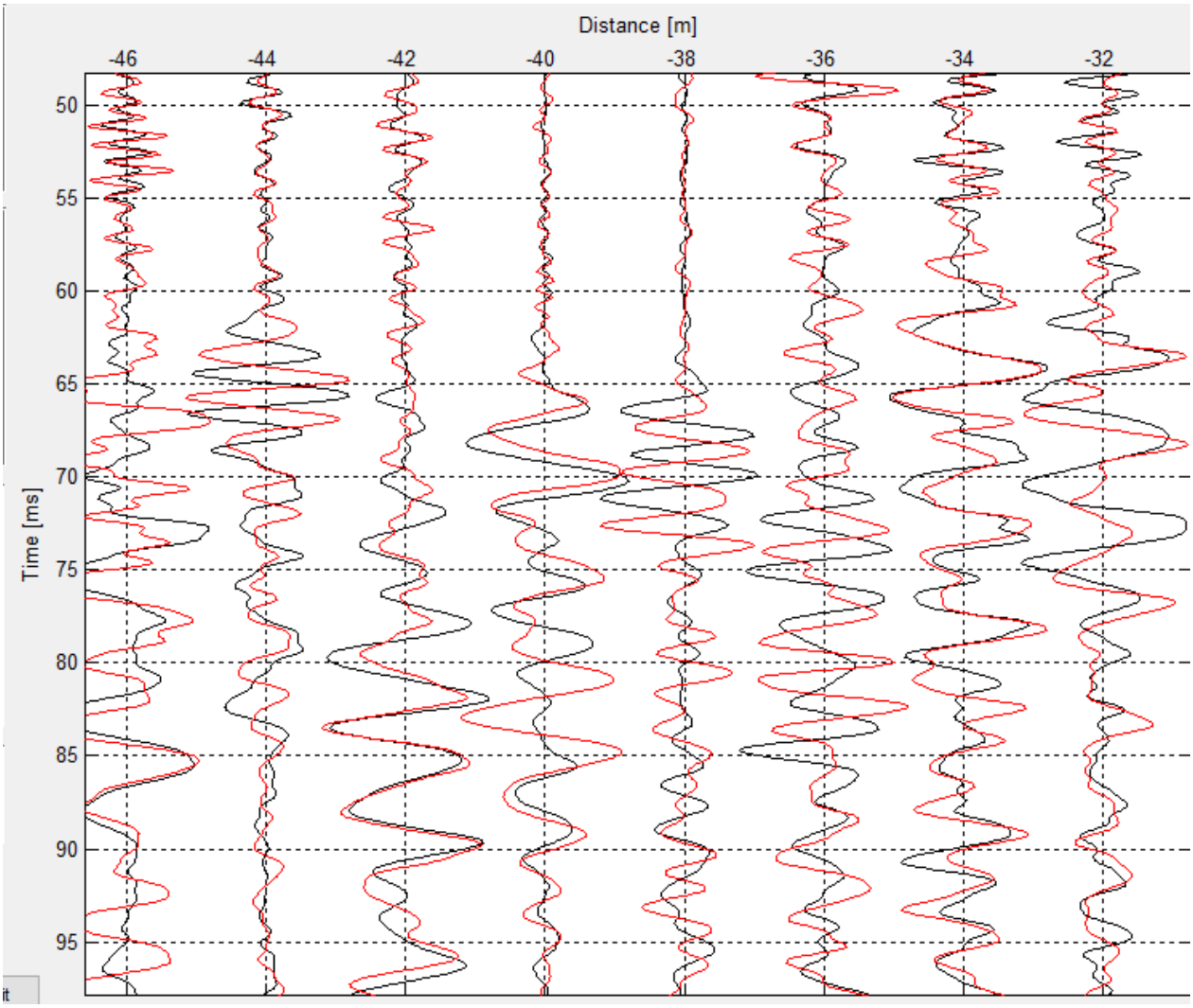

Figure 4: Example for varying signal quality for SH- waves at a depth range of 32 m to 46 m below surface. For instance, while the signal quality for 38 m is very high, the signal quality for 32 m is very low.

Since the signal quality of the S-wave varies enormously over the depth depending on the geology, the first arrival times could not be determined with the same accuracy for all depths. In the case of poor signal quality, neither the polarity change of the S-wave nor its typical wavelet could be clearly identified. As the signal quality decreases, the pick accuracy also decreases. In order to be able to quantify the inaccuracy of the first arrival times, a time range was defined for each pick using positive and negative time limits in which the S-wave arrives.

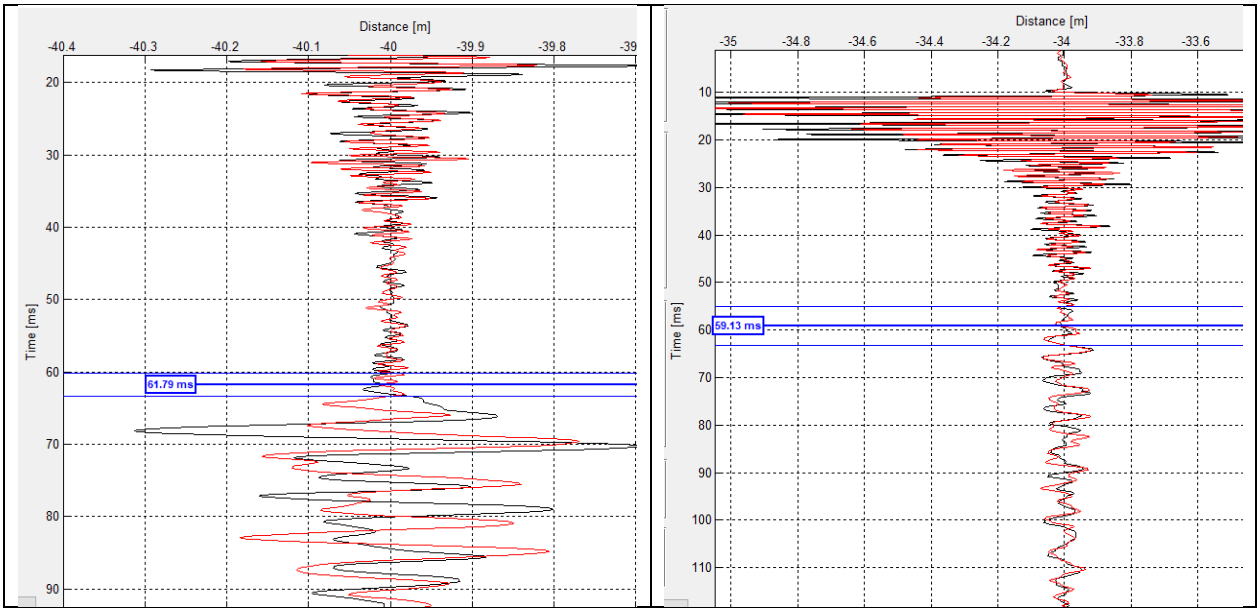

Figure 5: Signal examples at a depth of 40 m and 34m below the surface. (left) The left example shows a clear reversed polarity change. The blue line marks the determined first arrival time of the S-wave with an inaccuracy of +/- 1.57 ms. (right) The signal quality at the right example is not as good due to not clear polarity changes. The blue line marks the determined first arrival time of the S-wave with an inaccuracy of +/-4.1 ms.

The positive and negative limits, defined in milliseconds during the picking process, were used to define the pick accuracy: The smaller the limits, the higher the pick accuracy. In order to be able to quantify the pick accuracy for the entire data set and evaluate the results based on the pick accuracy, the limits of each pick set in milliseconds can be calculated as a percentage. Following maximum limits can be defined to quantify the pick accuracy:

1. **limits of max 5%:** The signal quality is very good, and the pick could be determined precisely.
2. **limits of max. 10%:** Signal quality is good to moderate, i.e., the pick could be determined with a minor inaccuracy.
3. **limits of >10%:** Signal quality is moderate to poor. The first arrival time of the S-wave could only be determined within a large time window and is therefore subject to more significant inaccuracy.

This procedure should be incorporated into the data processing of conventional and DAS data. It is not further discussed in this deliverable.

4 Example for assessing up-lift phenomena

4.1 Test site in Svelvik

Svelvik CO2 Field Lab is a small-scale laboratory established in the glaciofluvial-glaciomarine Holocene deposits of the Svelvik ridge and occupies a non-active part of sand and gravel quarry in the other part of Drammensfjorden. It is located about 50km southwest of Oslo. Down to 30m, it consists of unconsolidated to weakly consolidated sand, followed by interlayered sand, silt, clay layers. This test site is located at the factory site of Svelviksand, the largest supplier of dried sand to the mortar industry in Norway. The location near Drammensfjorden assumed that the tidewater level changes would influence the measurements.

Figure 6 : Location of the Svelvik CO2 Field Lab (Source: https://eccsel.org/media/111430/eccsel-eric-fact-sheet-no312-svelvikco2fieldlab.pdf)

4.2 Monitoring setup

The Svelvik CO2 Field Lab consists of an injection well and four monitoring wells. The injection well is designed for injecting CO2 and is equipped with a screen at 64-65 m depth. The four monitoring wells are approximately 100 m deep and positioned at the corners of a rhombus with the injection well in the center. The monitoring wells are located at 9.9 m (M3 and M4) and 16.5 m (M1 and M2) from the injection well. The section between M1 and M2 is oriented in the E.W. direction, while the section between M3 and M4 is oriented in the N.S. direction.

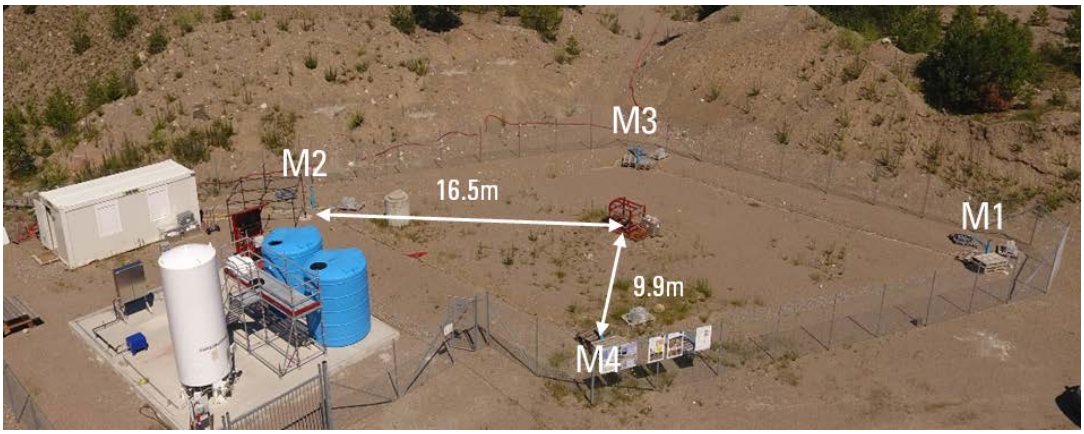

Figure 7: Svelvik CO2 Field Lab with injection (center) and monitoring wells (M1-M4) marked.

The seismic sources were placed in M4 sources and the seismic receiver in M3 for all experiments. To generate seismic signals, three different borehole sources were used. The borehole source type SBS42 (Geotomographie GmbH) generates P-waves. The BIS-SH (Geotomographie GmbH) generates mainly SH-waves and a good amount of P-waves. The novel borehole source type BIS-SV (Geotomographie GmbH) was used to generate SV-waves. Both source modes of operation of BIS-SH and BIS-SV were similar in that a solenoid was activated by high voltage and pushed either a copper plate against the borehole wall to generate a SH-wave impact or pushed the plate up and down to generate SV- waves. During operation, the source was pneumatically clamped to the borehole wall. The SH-probe is rotated by a torsionally stable and steel-reinforced tube. This ensures that the shear wave inserts are well-identified due to the reverse polarization of the S-waves during the 180° rotation. In contrast, excitation of SV-waves

is accomplished by an axial pulse force of the probe attached to the borehole wall and does not require any particular orientation of the probe for a second borehole. Due to a specially designed probe construction, sonic excitation in a second direction is possible, and thus rotation of this SV-probe in the borehole is no longer necessary.

Also, for the shear wave measurements, a Multistation-Borehole-Acquisition-System (MBAS) was used to receive P- and SH/SV-waves in the boreholes. The MBAS is a three-component geophone string and was re-designed to meet the environmental requirements at Svelvik. The MBAS consists of 8 receiver stations, each containing three geophone sensors in a tri-axial arrangement. The stations are aligned to ensure that all horizontal sensors are oriented in the same direction. Each station was clamped to the borehole wall by an air packer.

The crosshole tomographic S-wave measurements were conducted below the water table in two different depth zones with a source interval of 2m. In the deep zone with a depth range of 58m to 72m and the upper zone ranging from 32m to 46m. The P-wave measurements reach a depth range from 30 to 77m below the surface.

4.3 Auxilary data for data interpretation

Pressure and temperature are measured at the injection depth at the test site. Scintef made the following data available to the project DigiMON: Temperature and Pressure measurements measured at the boreholes M1, M2, M3 and the reference atmospheric pressure. Also, water level observation to assess the tidewater changes in Drammen were downloaded from https://www.kartverket.no/en/at-sea/se-havniva/result/?id=124591#waterlevel-tab. Geotomographie GmbH measured the borehole deviation at each borehole.

4.4 Data processing steps

First, the data sets of the P- and S-wave measurements were sorted, rotated to the shooting position and assigned to the measurement depths and the crosshole datasets were created from the tomographic dataset for each wave type.

For further analysis, the first arrival traveltimes for all wave types (P, SH and SV) were picked for each crosshole source and receiver configuration and velocities were calculated based on source and receiver distances. P-wave arrival times were determined by manually setting time markers for the fastest wave onset per measurement depth. The P-wave (first arrival) is clearly recognizable at all measurement depths and could be determined for all depths. In general, the P-wave should not be subject to a polarity change, while shear waves reverse polarity when the energy source polarity is reversed. Therefore, the S-wave can usually be determined with the help of the software superposition of the data sets by the separation of the signals and arrival times could be picked.

Then the picked arrival times were used for further data analysis. No inversion was carried out during that processing. Normalized data were calculated in comparison to the baseline data.

$$\text{Normalization} = \frac{Day_x - Baseline}{Baseline} * 100$$

A graph with these normalized velocity changes shows the temporal variation in seismic velocities at the test site.

4.5 Results and interpretation

Several studies reported a P-wave velocity decrease due to pressure increase during CO_2 injection. The P-wave data also show these characteristics in all depths within -30 to -77m. Especially on Day 3 and Day 4 (Figure 8, right), a maximum decrease (5-6%) of the normalized P-wave velocity data in relation to the baseline data can be seen in depth 38 and 39 m. The uncertainty in this data are mostly related to the instrument and picking error and it is estimated to be approximately 5% and does not change the overall depth related velocity distribution.

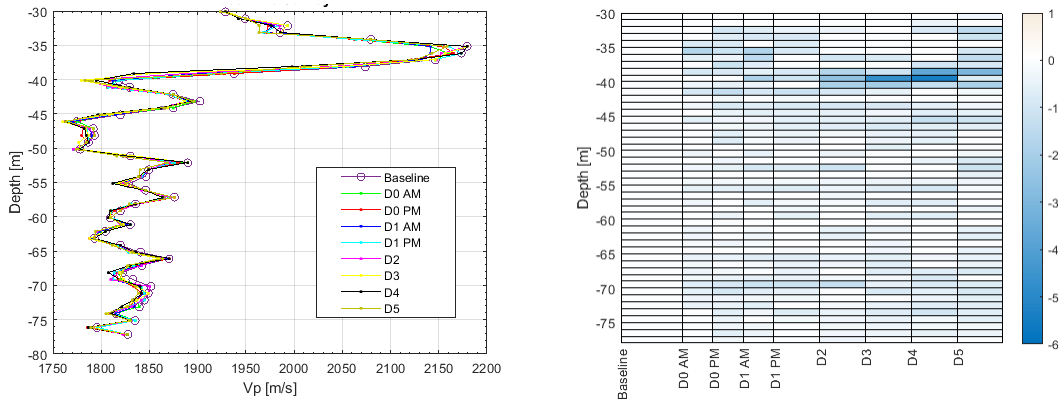

Figure 8: (left) V_P velocity profile from crosshole data and (right) temporal change of normalized P-wave velocity in relation to baseline

Apart from P-wave velocity changes also, changes in amplitudes can be expected. This amplitude change is assumed due to changes in the velocity changes of the reservoir induced by the injection. These velocity changes can also change the propagation time for seismic waves traveling through the reservoir. Figure 9 shows the seismic traces of two different depths for different time steps. It indicates that in depth 38 m below the surface a shift of the maximum of the amplitude is seen while in depth 43m below the surface the time and maximum of the amplitude for different time steps reveals constant.

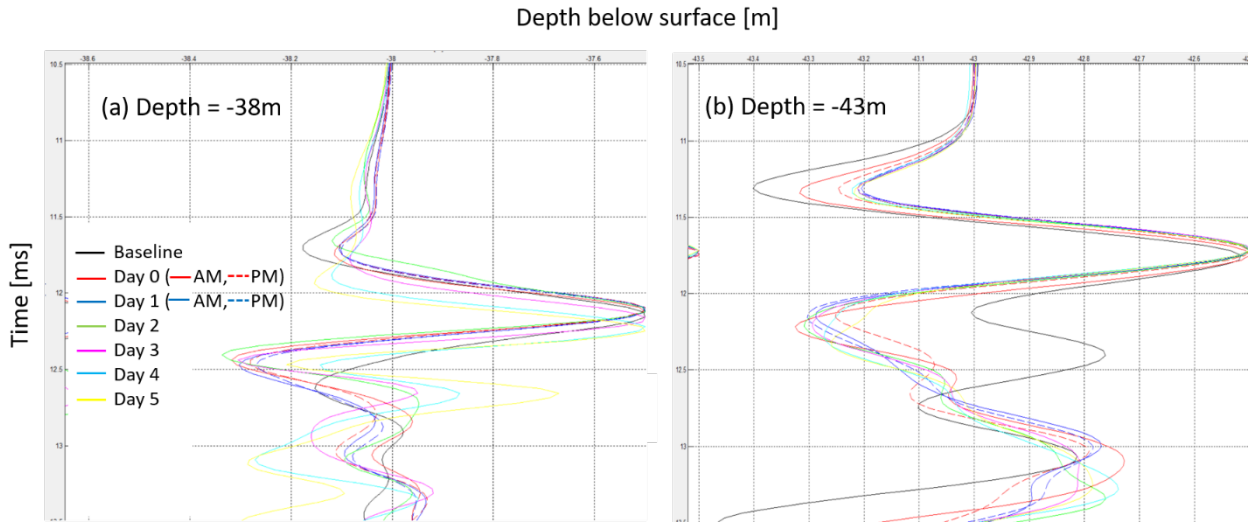

Figure 9: (a) Seismic trace of P-wave for a depth of 38m below surface for the different time steps. At this depth, a amplitude shift is recognizable while the amplitude maximum is nearly constant (b) Seismic trace of P-wave for a depth of 43m below surface, At this depth the amplitude does not vary in time and maximum at all leding to the conclusion that nothing happened at this depth

The literature states that shear waves behave similarly to P-waves but we could not source reliable results or publications.

The SH- and SV wave velocity profiles for the baseline, Day 0 and Day 1 are displayed in Figure 10 . All three time steps show a distinct zone between 62 m to 66 m below the surface where the SH- and SV- wave velocities differ and run apart.

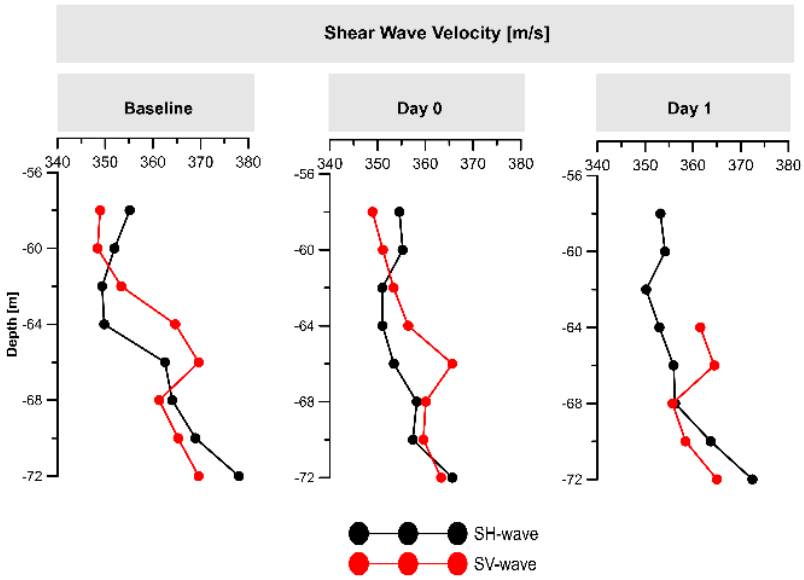

Figure 10: SH- and SV Wave velocities at different time steps baseline, Day 0, Day 1

Takano et al. (2014) reported seismic velocity changes due to the tide effects. Therefore, with its water level changes, the tide hub could influence the seismic measurements at the Svelvik test site to some extent, and consequently, there could be a superposition of the signals from both the effect of the tide hub and the CO_2 injection. It is a huge challenge to characterize the influence of the tide hubs on the signals because the measurement planning, unfortunately, did not consider the different tide cycles. We first examined the measurement times in relation to the tidal cycle and plotted them in Figure 11.

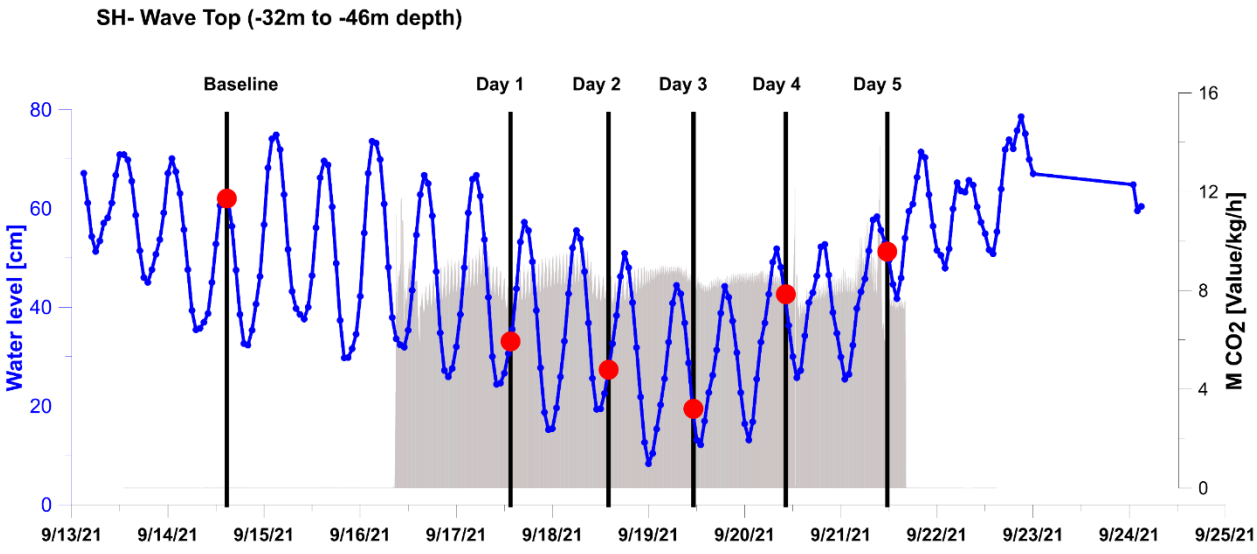

Figure 11: Temporal tide hub change and representation of the time of the measurement for VSH measurements at a depth range of -32 m –46 m

Figure 11 indicates that the tide difference between baseline measurements and measurements at Day 5 was very small and the tide difference between baseline measurements and measurements at Day 3 was very large. To analyze these effects, normalized data were calculated compared to the baseline data, as explained in chapter 3.4.

Figure 12 showes on the left side the V_{SH} velocity profile from crosshole data and on the right side the temporal change of normalized SH wave velocity in relation to baseline data. The velocity profile indicates that the SH-wave velocity decreases with each step compared to the baseline as reported in the literature.

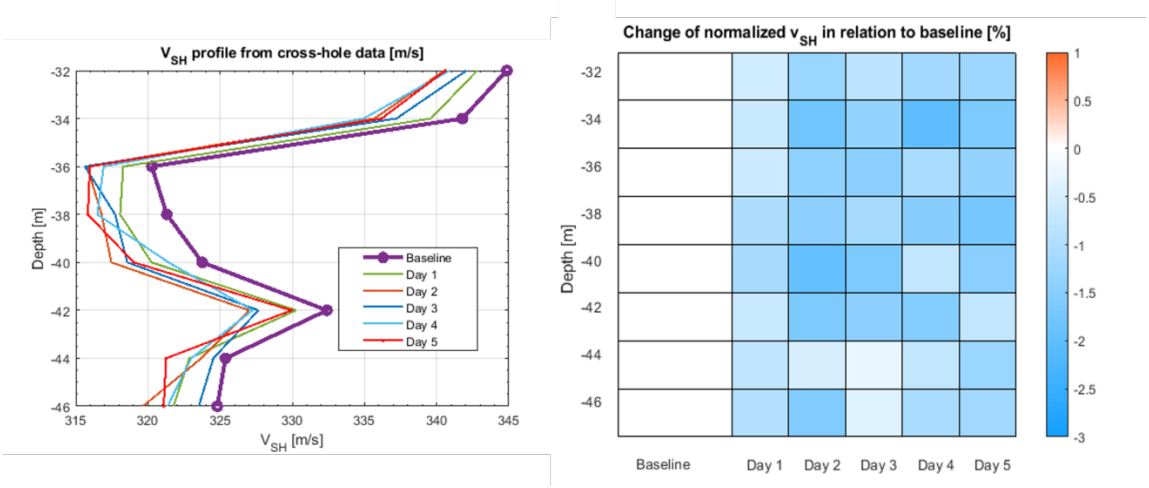

Figure 12: (left) V_{SH} velocity profile from crosshole data and (right) temporal change of normalized SH wave velocity in relation to baseline

Figure 13 displays the normalized SH-wave velocity changes to normalized water level changes for depth -32 to -46 m. The two blue dots indicate small Δwater level to baseline (small dot) and Δwater level to baseline large (large dot). It can be seen that the difference between these two dots is minimal for most of the depths. The difference is slightly enlarged for depth 42 m to 46 m (about 1% of the normalized data). The overall temporal behavior of this relationship is comparable for the upper depth range from 32 m to 30 m below the surface, showing a decrease between Day 0 and Day 1 and a slight increase to Day 2 followed by a decrease to Day 4 and Day 4. The temporal behavior changes in depth 40 m below the surface; there is a gradual increase between Day 3 to Day 4, followed by a decrease to Day 5. At 42 m, the behavior is similar; however, there is a decrease between Day 3 and Day 4 and an increase afterward. In the following two measured depths (42m and 44m below the surface), an almost excellent linear correlation between the normalized SH-wave velocity changes to normalized water level changes (tide). Therefore, deriving an overall relationship from these data is very complex due to this different temporal behavior.

At this point it is unlikely to quantify a tidal effect on changes in seismic velocity. Most likely all changes are related to the CO_2 injection as no dependency between tidal effect and changes in S-wave velocity was observed.

Figure 14 shows the seismic traces for the different time steps and depths. The amplitude characteristics are not as straightforward as for the P-wave. In depth 38 m and 42 m below the surface, we recognize a variation in the seismic traces. Also, analyzing the amplitude shifts and maxima we see a shift of the amplitude maxima.

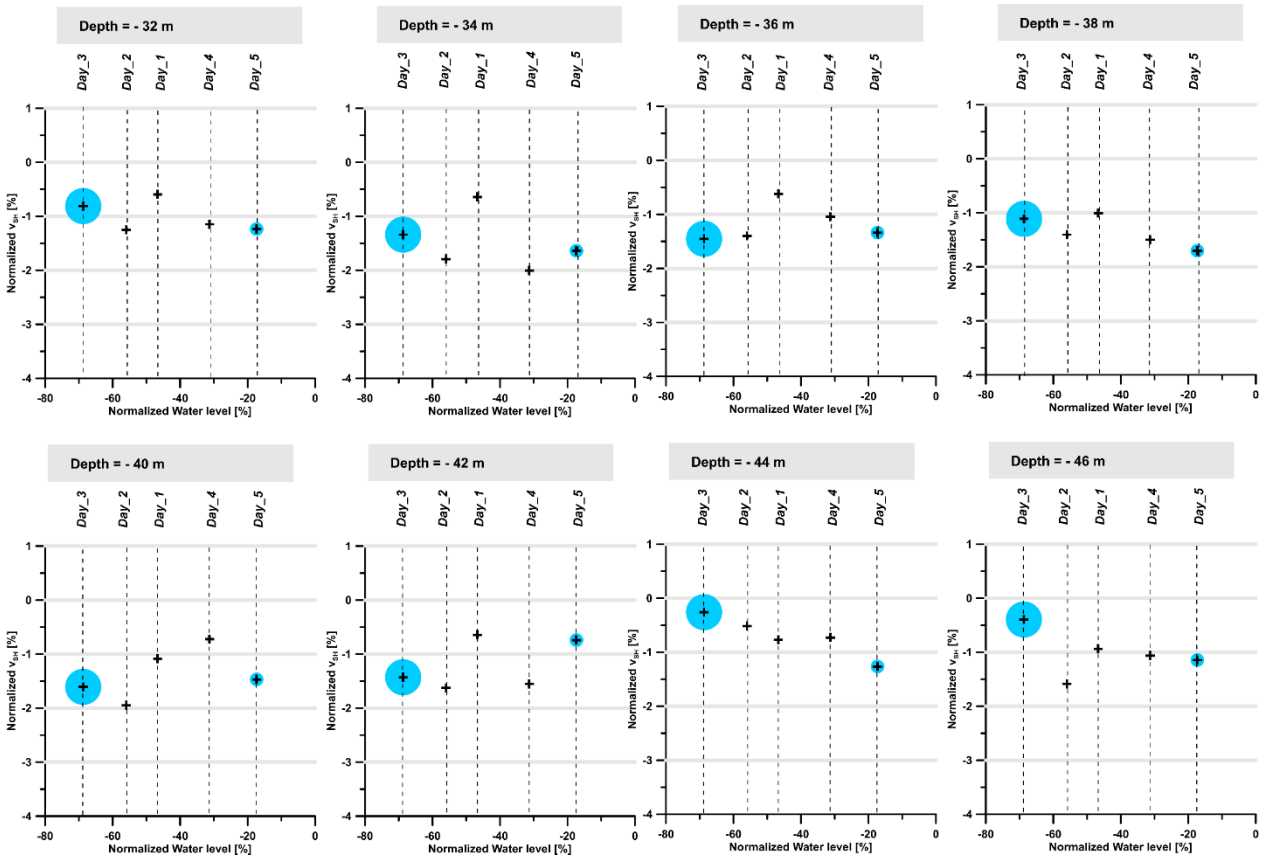

Figure 13: Normalized SH wave velocity changes to normalized tide hub changes for depth -32 to -46 m, blue dot small Δtidewater level to baseline small, blue dot large Δtidewater level to baseline large

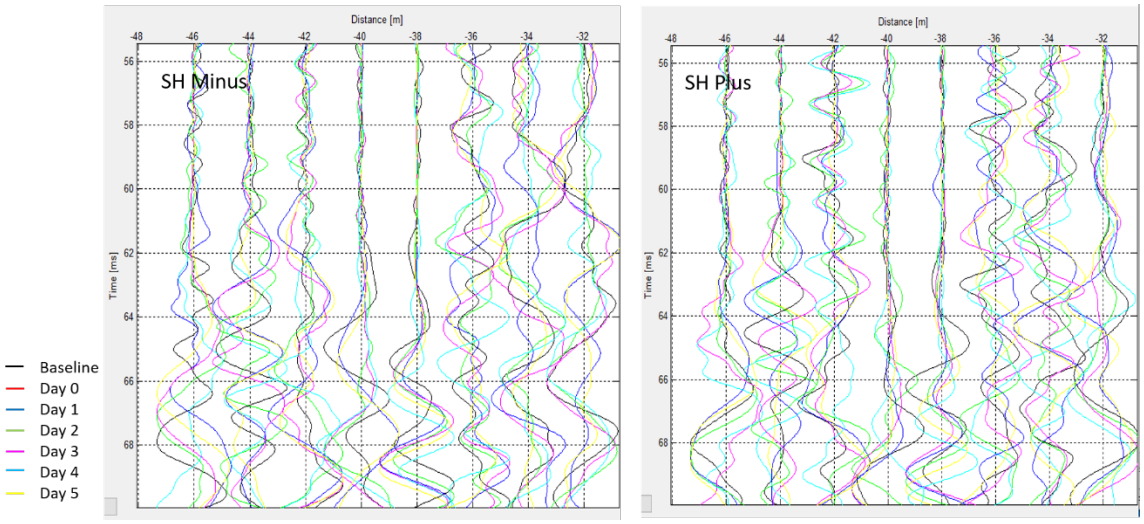

Figure 14: Recorded seismic traces of SH-wave for the different time steps and depths and the two polarization directions (SH – Minus, SH- Plus)

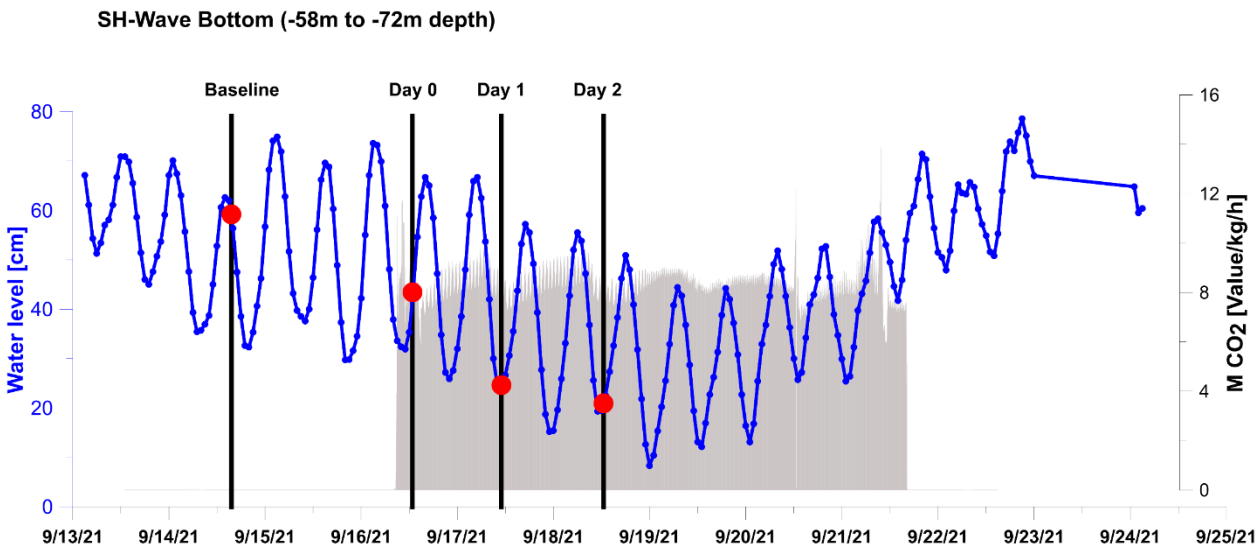

Figure 15: Temporal tide hub change and representation of the time of the measurement for V_{SH} measurements at a depth range of -58 m to -72 m

Figure 15 shows the temporal tidewater change and representation of the measurement time for V_{SH} measurements at a depth range of -58 m to -72 m. It can be seen that the Δ tidewater level was only significant in relation to the baseline at Day 2. Measurements with slight differences were not made. The temporal change of normalized SH-wave velocity in relation to baseline data shows a 2-3% decrease in the depth 70 m and 72 m below the surface and a smaller decrease at depth 66 m and 68 m below the surface (Figure 16,17). It seems that there are some changes in pressure in that depth caused by the injection. However, we could not explain that change in detail. In depths 70 and 72m below the surface, we also can recognize significant variations of the normalized SH-wave velocity changes. Especially between Day 0 and Day 1, there is an increase, followed by a decrease to Day 2. We assume that this effect is related to a pressure increase in that zone.

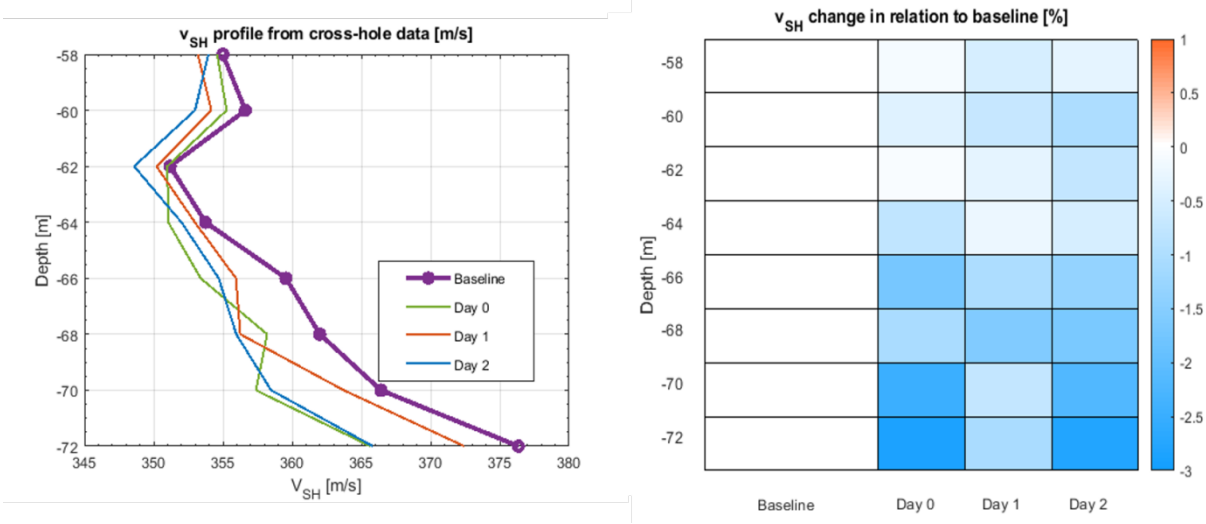

Figure 16: (left) V_{SH} velocity profile from crosshole data and (right) temporal change of normalized SH wave velocity in relation to baseline depth range of -58 m to -72 m

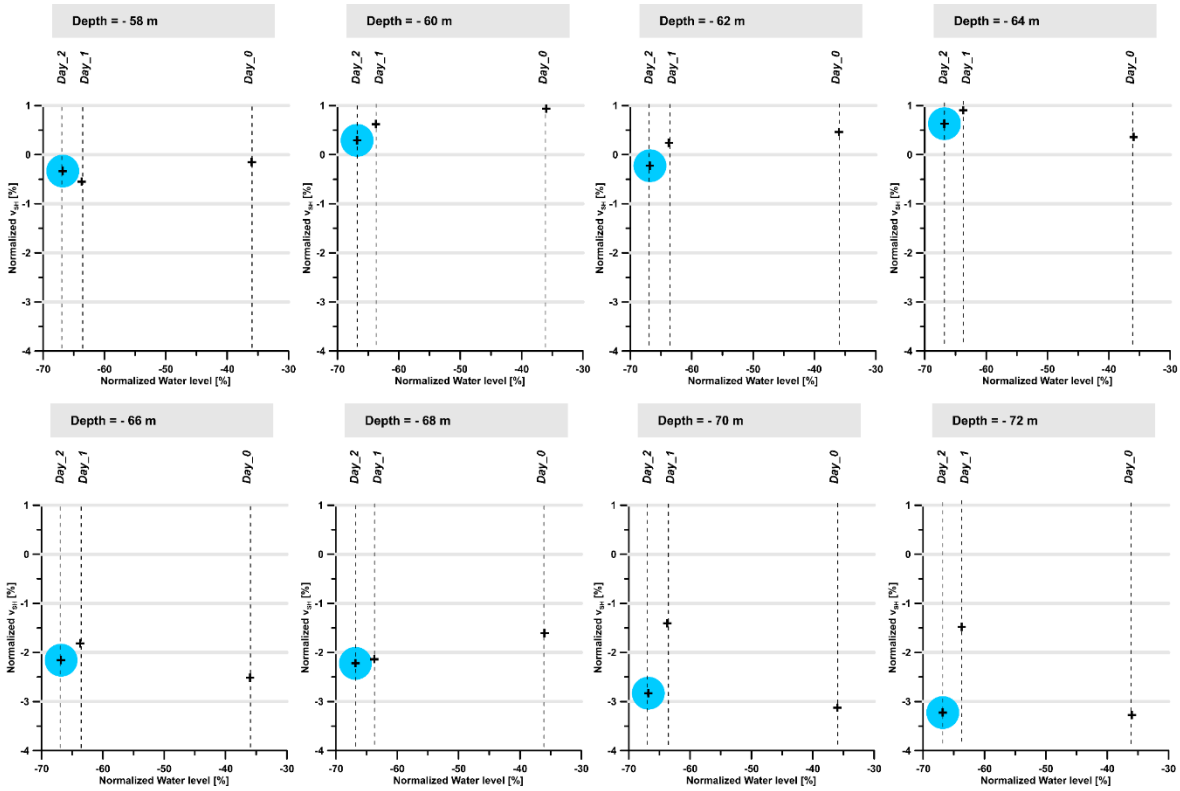

Figure 17: Normalized SH-wave velocity changes to normalized tide hub changes for depth -58 to -72 m, blue dot large indicates that Δtidewater level to baseline is large

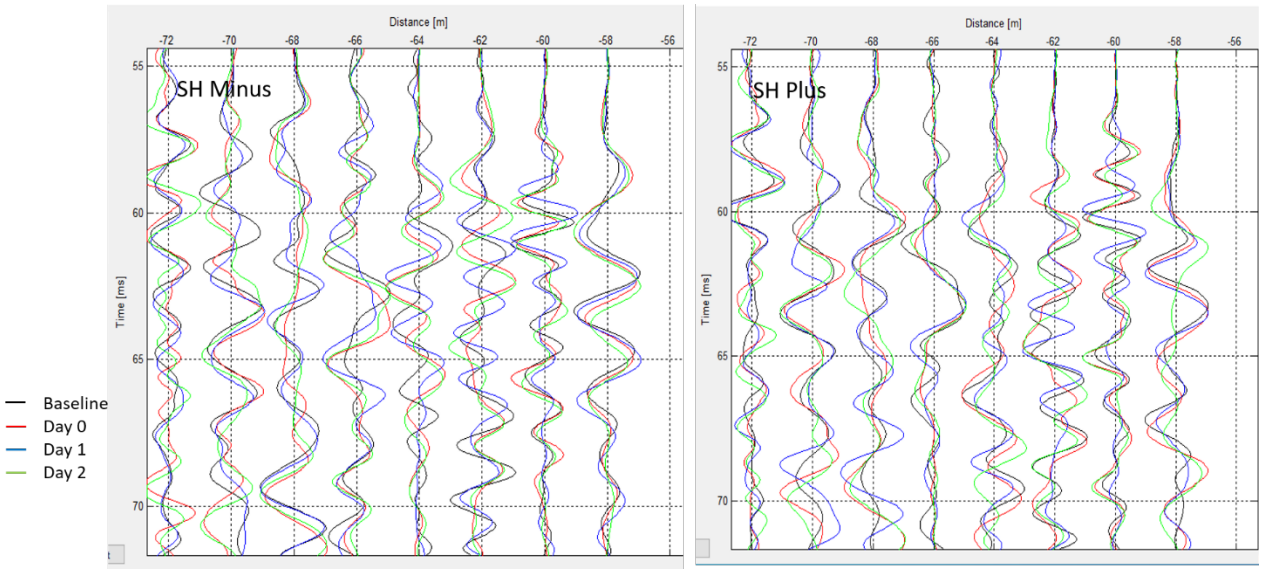

Figure 18: Recorded seismic traces of SH-wave for the different time steps and depths and the two polarization directions (SH – Minus, SH- Plus)

In FFigure 18, the recorded seismic traces of SH-wave for the different time steps and depths and the two polarization directions. There is no change in the maximum amplitude; only a shift of the maximum amplitude between the different time steps can be recognized in varying degrees at all depths. At 64 m below the surface, the most remarkable amplitude shift can be seen (see Figure 19), assuming a change in the subsurface conditions.

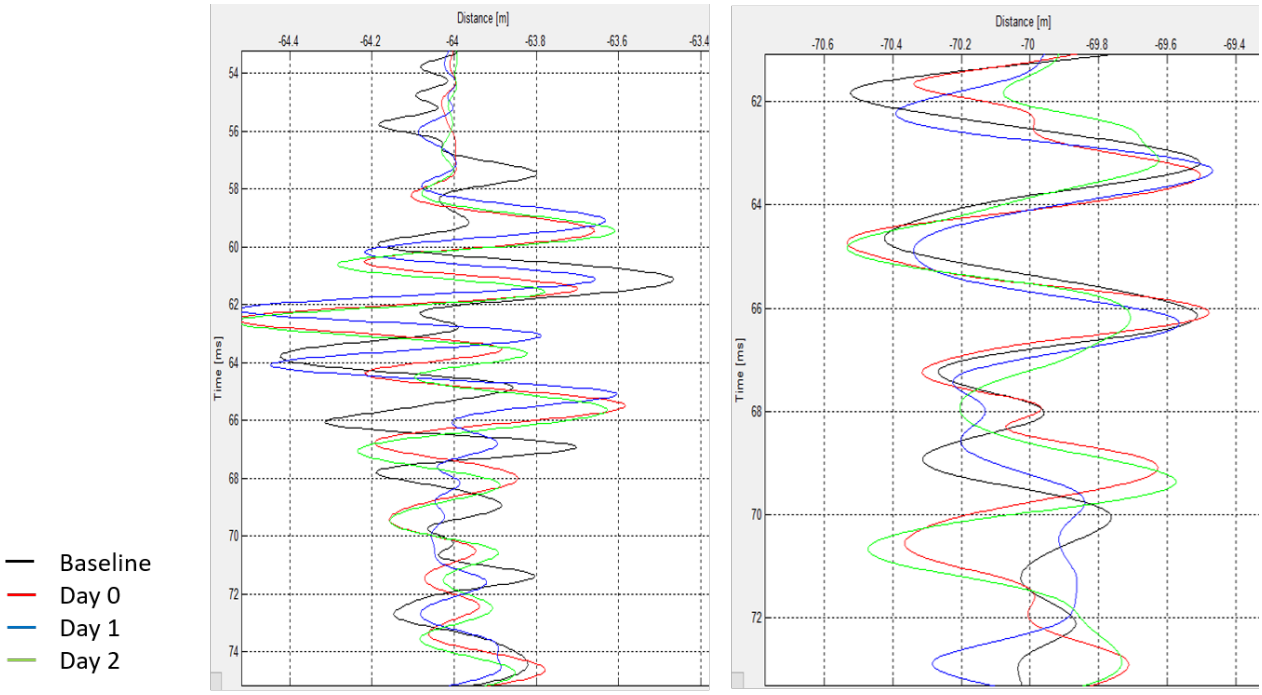

Figure 19: Recorded seismic traces of SH-wave for the different time steps and two depths below the surface (64 m and 70 m) in one polarization direction (SH – Minus)

In addition to the SH-waves, SV-waves were recorded using the novel SV- source (BIS-SV). As explained before, due to a specially designed probe construction, sonic excitation in a second direction is possible, and thus rotation of this SV-probe in the borehole is no longer necessary. Unfortunately, the inner driving coil system was damaged (short between adjacent copper layers) and the SV-source could not longer be used after three days of operation. Therefore, we rely on that three days datasets to make some interpretations.

Figure 20 shows the temporal tidewater change and representation of the SV-wave measurement time for V_{SH} measurements at a depth range of -58 m to -72 m. It can be seen that the Δ tidewater level was significant in relation to the baseline at Day 1. Measurements with slight differences were not made.

The temporal change of normalized SH-wave velocity in relation to baseline data shows reductions below depth 64 m with different extents (Figure 22). The most significant decrease is seen at depth 64 m below the surface on Day 0. This result confirms the assumption that the injection results in a change in the subsurface condition. In Figure 23 it can be seen that especially in depth 64 m below the surface a significant amplitude shift can be seen.

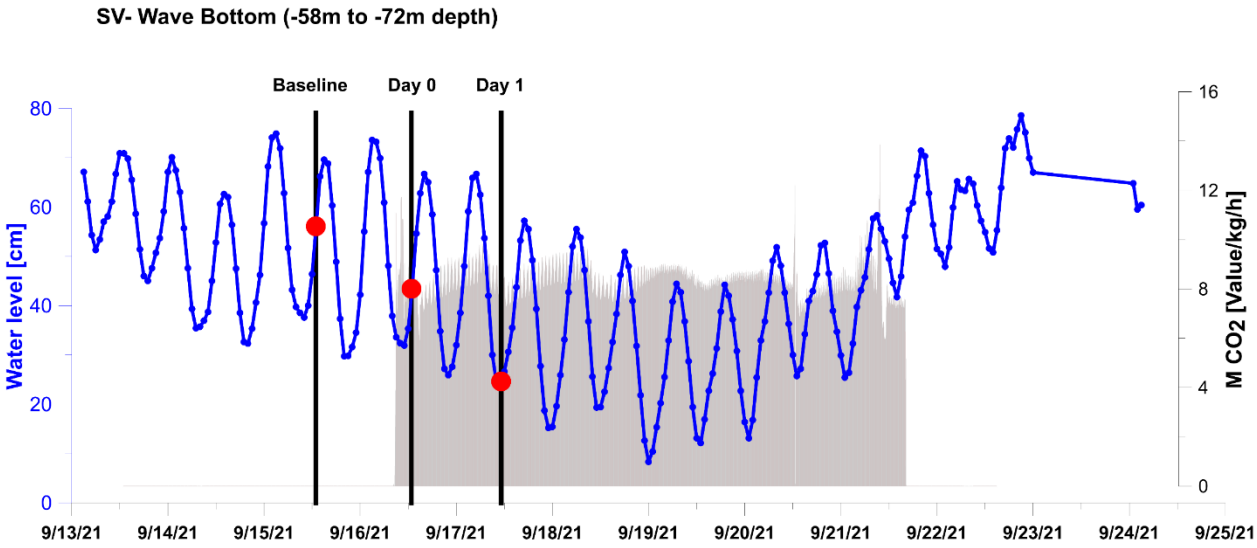

Figure 20: Temporal tide hub change and representation of the time of the measurement for V_{SV} measurements at a depth range of -58 m to -72 m

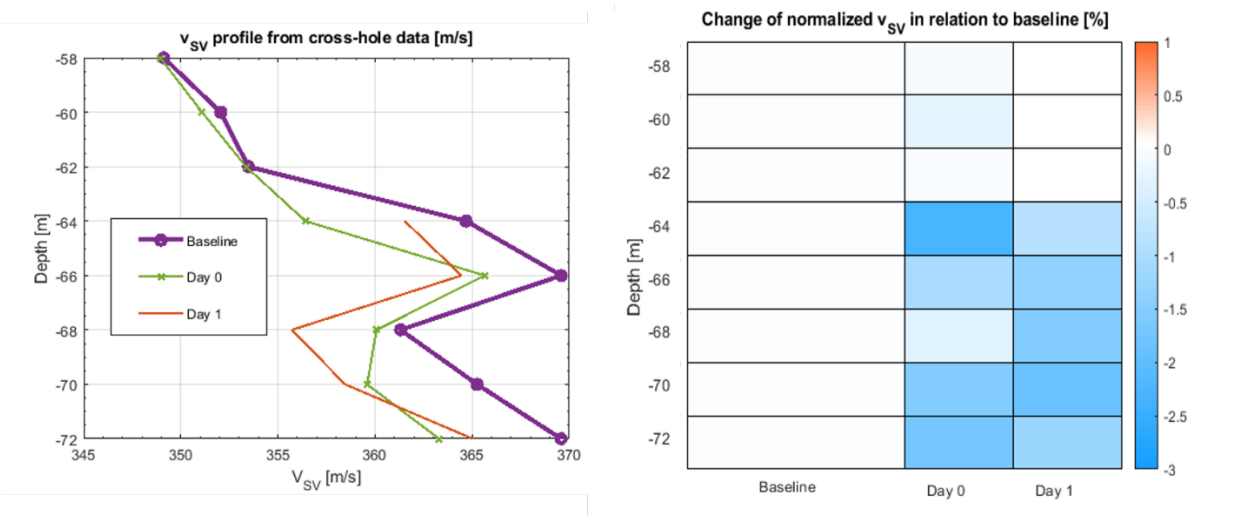

Figure 21: (left) V_{SV} velocity profile from crosshole data and (right) temporal change of normalized SV wave velocity in relation to baseline depth range of -58 m to -72 m

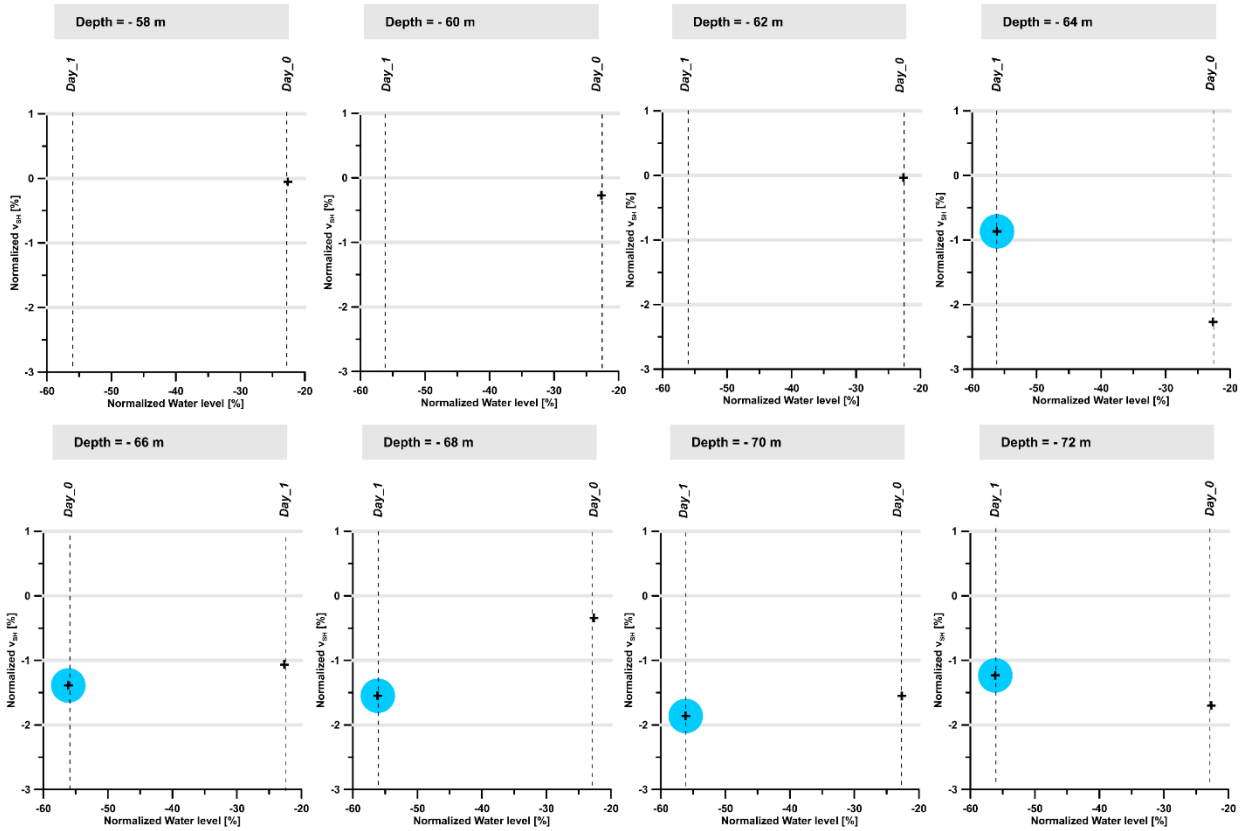

Figure 22: Normalized SV-wave velocity changes to normalized tide hub changes for depth -58 m to -72 m, blue dot large Δtidewater level to baseline large

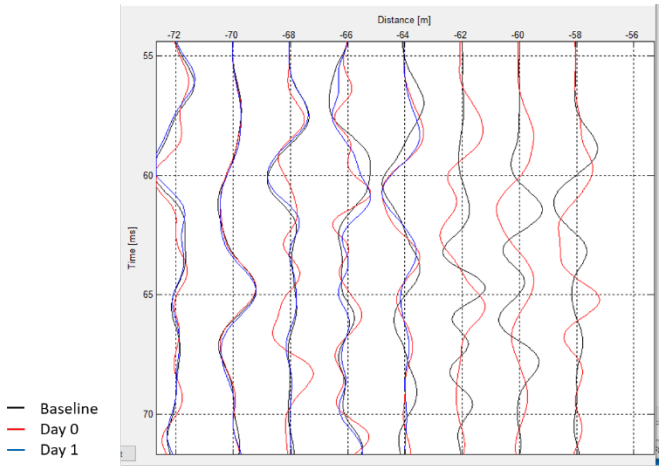

Figure 23: Recorded seismic traces of SV-wave for the different time steps and depths

It was assumed that uplift or other phenomena could be identified in the SH/SV ratio or the overconsolidation ratio or overconsolidation difference. Both parameters were calculated with the measured data and normalized to the baseline. The depth dependence of both parameters indicates a minimum at depth 64 m below the surface (Figure 24 and Figure 25-left). This depth also represents a vertex, i.e., above it, the parameter is more significant at the measurements

following the baseline measurement, while below it, the parameter decreases with time. Figure 24 and 25 right display the temporal change of the normalized parameter (SH/SV ratio, OCD) in relation to baseline and show a distinct maximum at depth 64 m below the surface. We assume that in that depth, a change of subsurface condition occurred. Thus, the measured data allow the conclusion that the CO_2 injection effects the propagation of S-waves. It is assumed that this change of a few percent is most likely related to a change in local pore pressure situation and may effect the grain-grain contacts. An up-lift phenomenon cannot be quantified.

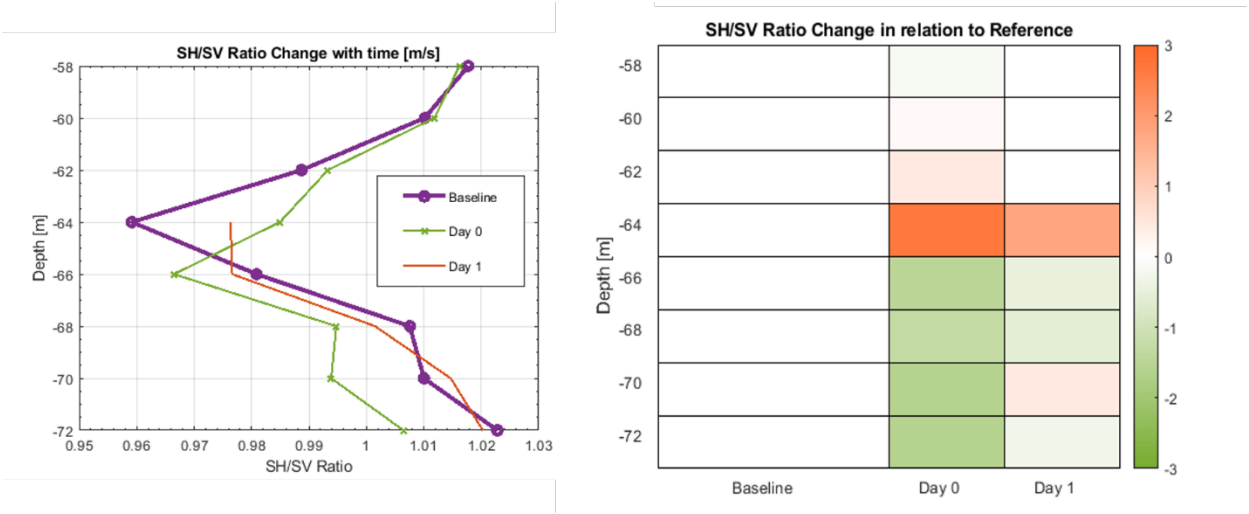

Figure 24: (left) V_{SH}/V_{sv} ratio profile from crosshole data and (right) temporal change of normalized SH/SV ratio in relation to baseline depth range of -58 m to -72 m

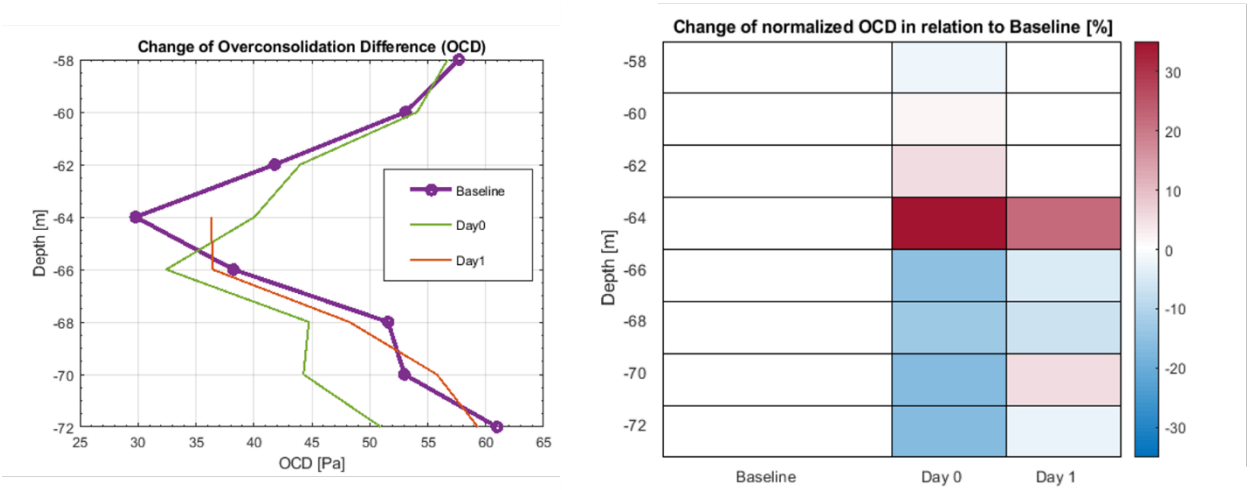

Figure 25: (left) OCD profile from crosshole data and (right) temporal change of normalized OCD ratio in relation to baseline depth range of -58 m to -72 m

5 Lessons learned for Digimon References

What conclusions can be made from this experiment:

- Tidewater changes have been superimposed on the effects due to CO_2 injection. Separation requires a measurement plan adapted to the tidal change, i.e., measurement at different tidal range times. A set up of a measurement plan that record the tidal effect at different time steps can help to find a correlation function between the tidal effect and S-wave changes. Simple assumptions are made in this deliverable but due to the very small effects it is not possible to separate clearly both effects.
- Also, a geological model is needed for interpretation and for separation both effects. This model helps to explain the S-wave changes.
- SH/SV ratio or OCD can make changes in the subsurface conditions visible. The temporal behavior of the derived parameters is coherent for the measured datasets. However, conclusions regarding uplift phenomena or stress-induced anisotropy can not be made.
- Field use of the novel SV probe revealed problems with sustained operation and allowed the construction to be modified.
- Pick accuracy is a primary factor of uncertainty. Therefore, the proposed approach described in chapter 2.3 should be used to quantify the accuracy.

6 References

Amelung, F.; Gallowey, D.L.; Bell, J.; Zebker, H.; Laczniak, R.J. (1999). Sensing the ups and downs of Las Vegas: InSAR reveals structural control of land subsidence and aquifer-system deformation. Geology 1999, 27, 483–486.

Amer, R.; Xue, Z.; Hashimoto, T.; Nagata, T. (2021). Distributed Fiber Optic Strain Sensing for Geomechanical Monitoring: Insights from Field Measurements of Ground Surface Deformation. Geosciences 2021, 11, 285. https://doi.org/ 10.3390/geosciences11070285

Arts, R., Chadwick, A., Eiken, O., Thibeau, S., & Nooner, S. (2008). Ten years experience of monitoring CO2 injection in the Utsira Sand at Sleipner, offshore Norway. First Break, 26, 91– 96.

Bateson, L.; Cigna, F.; Boon, D.; Sowter, A. (2015). The application of the Intermittent SBAS (ISBAS) InSAR method to the South Wales Coalfield, UK. Int. J. Appl. Earth Obs. Geoinf. 2015, 34, 249–257.

Boait, F., White, N. J., Bickle, M. J., Chadwick, R. A., Neufeld, J. A., & Huppert, H. E. (2012). Spatial and temporal evolution of injected CO2 at the Sleipner Field, North Sea. Journal of Geophysical Research, 117, B03309. https://doi.org/10.1029/2011JB008603

Bonì R, Bosino A, Meisina C, Novellino A, Bateson L, McCormack H. A (2018). Methodology to Detect and Characterize Uplift Phenomena in Urban Areas Using Sentinel-1 Data. Remote Sensing. 2018; 10(4):607. Doi: 10.3390/rs10040607

Bourne S, Crouch S, Smith M (2014) A risk-based framework for measurement, monitoring and verification of the Quest CCS project, Alberta, Canada. Int J Greenhouse Gas Control 26:109– 126. doi: 10.1016/j.ijggc.2014.04.026

Brake, B.T.; Hanssen, R.F.; Van der Ploeg, M.J.; De Rooij, G.H. (2013). Satellite-based radar interferometry to estimate large-scale soil water depletion from clay shrinkage: Possibilities and limitations. Vadose Zone J. 2013, 12.

Castellazzi, P.; Arroyo-Domínguez, N.; Martel, R.; Calderhead, A.I.; Normand, J.C.L.; Gárfias, J.; Rivera, A. (2016). Land subsidence in major cities of Central Mexico: Interpreting InSAR-derived land subsidence mapping with hydrogeological data. Int. J. Appl. Earth Obs. 2016, 47, 102–111.

Chadwick RA, Williams GA, Williams JDO, Noy DJ (2012) Measuring pressure performance of a large saline aquifer during industrial-scale CO2 injection: The Utsira Sand, Norwegian North Sea. Int J Greenh Gas Control 10:374–388,

Chaussard, E.; Milillo, P.; Bürgmann, R.; Perissin, D.; Fielding, E.J.; Baker, B. (2017). Remote Sensing of Ground Deformation for Monitoring Groundwater Management Practices: Application to the Santa Clara Valley During the 2012–2015 California Drought. J. Geophys. Res. Solid Earth 2017, 122, 8566–8582.

Costantini, M.; Ferretti, A.; Minati, F.; Falco, S.; Trillo, F.; Colombo, D.; Novali, F.; Malvarosa, F.; Mammone, C.; Vecchioli, F.; et al. (2017). Analysis of surface deformations over the whole Italian territory by interferometric processing of ERS, Envisat and COSMO-SkyMed radar data. Remote Sens. Environ. 2017, 202, 250–275.

Crane, J. M. (2013).Effects of stress and water saturation on seismic velocity and attenuation in near surface sediments, LSU Doctoral Dissertations. 3714.

Deffontaines, B.; Kaveh, F.; Fruneau, B.; Arnaud, A.; Duro, J. (2015). Monitoring Swelling Soils in Eastern Paris (France) through DinSAR and PSI Interferometry: A Synthesis. In Engineering Geology for Society and Territory; Lollino, G.,

Dong, J.; Zhang, L.; Liao, M.; Gong, J. (2019). Improved correction of seasonal tropospheric delay in InSAR observations for landslide deformation monitoring. Remote Sens. Environ. 2019, 233, 111370.

downloaded under https://digitalcommons.lsu.edu/gradschool_dissertations/3714 on February 24,2022

Duxbury A, et al. (2012) Fracture mapping using seismic amplitude variation with offset and azimuth analysis at the Weyburn CO2 storage site. Geophysics 77(17-N):28

Eiken, O. (2019). Twenty years of monitoring CO2 injection at Sleipner. In T. L. Davis, M. Landro, & M. Wilson (Eds.), Geophysics and Geosequestration. Dordrecht: Springer.
Galloway, D.L.; Jones, D.R.; Ingebritsen, S.E. (1999). Land Subsidence in the United States: U.S. Geological Survey; Circular 1182; U.S. Geological Survey: Reston, VA, USA, 1999; p. 177.
Gee, D.; Bateson, L.; Sowter, A.; Grebby, S.; Novellino, A.; Cigna, F.; Marsh, S.; Banton, C.; Wyatt, L. (2017). Ground motion in areas of abandoned mining: Application of the intermittent SBAS (ISBAS) to the Northumberland and Durham coalfield, UK. Geosciences 2017, 7, 85.
Gibson-Poole, C. M, & Raikes, S. (2010). Enhanced understanding of CO2 storage at Krechba from 3D seismic. In Proceedings of the 9th Annual Conference on Carbon Capture and Sequestration, Pittsburgh, PA, pp. 10– 13. May 2010.
Hatchell P, Bourne S (2005) Rocks under strain: Strain-induced time-lapse time shifts are observed for depleting reservoirs. Leading Edge (Tulsa Okla) 24:1222–1225.
Hatchell P, Bourne S (2005) Rocks under strain: Strain-induced time-lapse time shifts are observed for depleting reservoirs. Leading Edge (Tulsa Okla) 24:1222–1225.
Herwanger, J. and Horne, S. (2009). Linking reservoir geomechanics and time-lapse seismics: Predicting anisotropic velocity changes and seismic attributes. Geophysics. 74. 10.1190/1.3122407.
IEA (2012) Best practices for validating CO2 geological storage: observations and guidance from the IEAGHG Weyburn-Midale CO2 monitoring and storage project. Geoscience Publishing
INSIDE (2022). Stress redistribution from deep geothermal energy – aka "microseismicity, downloaded under https://inside-geothermie.de/en/02-background/#Induzierte-seismizitaet on February 14, 2022
James P. Verdon, J.-Michael Kendall, Anna L. Stork, R. Andy Chadwick, Don J. White, Rob C. Bissell (2013). Geomechanical deformation at CCS sites, Proceedings of the National Academy of Sciences Jul 2013, 110 (30) E2762-E2771; DOI: 10.1073/pnas.1302156110
Johnston, D.; Potter, H.; Jones, C.; Rolley, S.; Watson, I.; Pritchard, J. (2008). Environmental Agency Report. In Abandoned Mines and the Water Environment; Environment Agency: Bristol, UK, 2008.
Karegar, M.A.; Dixon, T.H.; Malservisi, R.; Yang, Q.; Hossaini, S.A.; Hovorka, (2015). S.D. GPS-based monitoring of surface deformation associated with CO2 injection at an enhanced oil recovery site. Int. J. Greenh. Gas Control 2015, 41, 116–126
Korneev,V,. Glubokovskikh,S. (2013).Seismic velocity changes caused by an overburden stress GEOPHYSICS 78: WC25-WC31. https://doi.org/10.1190/geo2012-0380.1
Ku, T., and Mayne, P.W., 2014, Stress history profiling in soils using OCD-G0 anisotropy relationship: Proceedings of the Institution of Civil Engineers, Geotechnical Engineering, 167, 476–490
Kurka, M.; Gutjahr, K.H. (2015). Observation of Expansive Clay Movement with DInSAR. G. In Engineering Geology for Society and Territory; Lollino, G., Manconi, A., Clague, J., Shan, W., Chiarle, M., Eds.; Springer International Publishing: Cham, Switzerland, 2015; Volume 5, pp. 151–154. ISBN 978-3-319-09048-1.
Landro, Martin & Veire, Helene & Duffaut, Kenneth & Najjar, Nazih. (2003). Discrimination between pressure and fluid saturation changes from marine multicomponent time-lapse seismic data. Geophysics. 68. 10.1190/1.1620633.
Liu, Y.; Liu, J.; Xia, X.; Bi, H.; Huang, H.; Ding, R.; Zhao, L. (2021). Land subsidence of the Yellow River Delta in China driven by river sediment compaction. Sci. Total Environ. 2021, 750, 142165.
Mackens, S., Hocine, Y. , Werban, Ulrike. (2017). Direct-push Based Seismic Crosshole Testing for Geotechnical Engineering Applications. Journal of Environmental & Engineering Geophysics. 22. 291-297. 10.2113/JEEG22.3.291.
Manconi, A., Clague, J., Shan, W., Chiarle, M., Eds.; Springer International Publishing: Cham, Switzerland, 2015; Volume 5, pp. 195–202. ISBN 978-3-319-09048-1.
Meyer, F.J.; McAlpin, D.B.; Gong, W.; Ajadi, O.; Arko, S.; Webley, P.W.; Dehn, J. (2015). Integrating SAR and derived products into operational volcano monitoring and decision support systems. ISPRS J. Photogramm. 2015, 100, 106–117.
Necsoiu, M.; Onaca, A.; Wigginton, S.; Urdea, P. (2016). Rock glacier dynamics in Southern Carpathian Mountains from high-resolution optical and multi-temporal SAR satellite imagery. Remote Sens. Environ. 2016, 177, 21–36.
Nicol, Andy & Seebeck, H. & McNamara, David & Field, B. (2016). Fault Permeability. IEA Environmental Projects Ltd. (IEAGHG) Report 2016/13 October 2016.
Olofsson B, Probert T, Kommedal JH, Barkved O (2003) Azimuthal anisotropy from the Valhall 4C 3D survey. Leading Edge (Tulsa Okla) 22:1228–1235
Onuma, T. & Ohkawa, S. (2009). Detection of surface deformation related with CO2 injection by DInSAR at In Salah, Algeria. Energy Procedia. 92. 2177-2184. doi: 10.1016/j.egypro.2009.01.283.
Roesler, S. (1979). Anisotropic shear modulus due to stress anisotropy: Journal of Geotechnical Engineering Division, 105, 871–880.
Staples R, Ita J, Burrell R, Nash R (2007) Monitoring pressure depletion and improving geomechanical models of the Shearwater field using 4D seismic. Leading Edge (Tulsa Okla) 26:636–642
Staples R, Ita J, Burrell R, Nash R (2007) Monitoring pressure depletion and improving geomechanical models of the Shearwater field using 4D seismic. Leading Edge (Tulsa Okla) 26:636–642.
Stork, Anna L., Verdon, James P. , Kendall, J.-Michael (2015). The microseismic response at the In Salah Carbon Capture and Storage (CCS) site, International Journal of Greenhouse Gas Control, Volume 32,159-171, https://doi.org/10.1016/j.ijggc.2014.11.014.
Takano, T., T. Nishimura, H. Nakahara, Y. Ohta, and S. Tanaka (2014), Seismic velocity changes caused by the Earth tide: Ambient noise correlation analyses of small-array data, Geophys. Res. Lett., 41, 6131–6136, doi:10.1002/2014GL060690.
Teatini, P. & Gambolati, G., Ferronato, M., Settari, A., Walters, D.. (2011). Land uplift due to fluid injection. Journal of Geodynamics. 51. 1-16. 10.1016/j.jog.2010.06.001.
Tromp, J., Marcondes, M. L., Wentzcovitch, R. M. M., & Trampert, J. (2019). Effects of induced stress on seismic waves: Validation based on ab initio calculations. Journal of Geophysical Research: Solid Earth, 124, 729– 741. https://doi.org/10.1029/2018JB016778
Verdon, J. P., Kendall, J.-M. Kendall, Stork, A. L., Chadwick, R. A., White, D. J.; Bissell, R. C. (2013). Geomechanical deformation at CCS sites, Proceedings of the National Academy of Sciences Jul 2013, 110 (30) E2762-E2771; DOI: 10.1073/pnas.1302156110
White, D. J. (2013a). Toward quantitative CO2 storage estimates from time-lapse 3D seismic travel times: An example from the IEA GHG Weyburn-Midale CO2 monitoring and storage project. International Journal of Greenhouse Gas Control, 16S, S95– S102.
White, D. J. (2013b). Seismic characterization and time-lapse imaging during seven years of CO2 flood in the Weyburn field, Saskatchewan, Canada. International Journal of Greenhouse Gas Control, 16S, S78– S94.

White, D. J., Meadows, M., Cole, S., Ramirez, A., Hao, Y., Carle, S., Duxbury, A., Samson, C., Kendall, J. M., Verdon, J. P., Dietiker, B., Johnson, J., & Morozov, I. (2011). Geophysical monitoring of the Weyburn CO2 flood: Results during 10 years of injection. Energy Procedia, 4, 3628– 3635.
White, D. J., Roach, L. A. N., & Roberts, B. (2015). Time-lapse performance of a sparse permanent array: Experience from the Aquistore CO2 storage site. Geophysics, 80, WA35– WA48.
Winterstein, D. F., and Meadows, M. A. (1991). Shear-wave polarization and subsurface stress directions at Lost Hills field: Geophysics, 56, 1331–1348
Zhang, R., Vasco, D. W., Daley, T. M., & Harbert, W. (2015). Characterization of a fracture zone using attributes at the In Salah CO2 storage project. Interpretation, 3, SM37– SM46. https://doi.org/10.1190/INT-2014-0141.1
Zhang, Z.; Wang, C.; Tang, Y.; Fu, Q.; Zhang, H. (2015). Subsidence monitoring in coal area using time-series InSAR combining persistent scatterers and distributed scatterers. Int. J. Appl. Earth Obs. 2015, 39, 49–55.
Zuo, J.; Gong, H.; Chen, B.; Liu, K.; Zhou, C.; Ke, Y. (2019). Time-Series Evolution Patterns of Land Subsidence in the Eastern Beijing Plain, China. Remote Sens. 2019, 11, 539.